Naturally occurring 2D semiconductor with antiferromagnetic ground state

Check for updates

Barbara Pacakova[1] ✉, Bera Lahtinen-Dahl[1], Alexsandro Kirch[2], Hanna Demchenko[1], Veslemoy Osmundsen[1], Chloe A. Fuller[3], Dmitry Chernyshov[3], Dominika Zakutna[4], Caetano R. Miranda[2], Steinar Raaen[1] & Jon Otto Fossum[1] ✉

The natural clay mineral vermiculite has been overlooked as a promising candidate for scalable production of large aspect ratio 2D wide band-gap semiconductors. We combine here efficient methods for vermiculite delamination, which provides single nanosheets of ~1 nm thickness. It is demonstrated by experiments and simulations that delaminated vermiculite nanosheets act as semiconductors with a wide band-gap energy of 3.3–3.9 eV depending on the elemental composition, and with an antiferromagnetic ground state, which is crucial for creating advanced 2D devices operating at high frequencies or voltages. This study advances the understanding of vermiculite. With its natural abundance, affordability, non-toxicity, and ability to form high-quality nanosheets, vermiculite is a valuable and sustainable resource for future electronic, spintronic and photonics devices.

The natural and abundant clay mineral vermiculite is a hitherto unexplored candidate for upscaled fabrication of large aspect ratio 2D antiferromagnetic wide band-gap semiconductors or insulators. Vermiculite delamination into single nanosheets has been considered a difficult task, mainly due to their high negative layer charge, as well as the presence of non-hydratable interlayer charge compensating cations, such as potassium.

Here we report successful exchange with Na^+ cations, partly or fully replacing original interlayer cations such as K^+ and Mg^{2+}, for 12 different versions of sourced natural vermiculite. Use of different organic solvents followed by mechanical treatment allow for delamination into single 0.95 nm thin 2D vermiculite nanosheets.

We find evidence both from the simulations and experiment that these vermiculite nanosheets are 2D semiconductor antiferromagnets, with a band gap energy value approximately $E_g = 3.3$–3.9 eV, depending on the elemental composition.

Due to this relatively wide band gap in comparison with wide band gap synthetized semiconductors, we conclude that vermiculite indeed must be seriously explored for use in large volume production of future nano-electronic and photonic devices[1]. Moreover, the antiferromagnetic properties of these large aspect ratio nanosheets may enable spintronic applications beyond current technological capabilities.

In electronic devices, it is essential to combine the magnetic state of 2D layers with their semiconducting properties, especially for wide band gap materials. Wide band gap semiconductors provide significant potential for applications, such as in high temperature and high-speed electronics, operating at increased electric fields and switching frequencies, resisting high breakthrough voltage[2,3]. These semiconductors can exploit a variety of spin-related phenomena that are not available in other materials. While most magnetic semiconductors are ferromagnetic, incorporating antiferromagnetic materials can significantly expand their application potential[4].

Most of the reported large band gap semiconductors are synthetic[2,3], where GaN is a typical example. For scaling up and ensuring the wide availability of 2D antiferromagnetic semiconductors, it is crucial to identify materials that are cheap and readily accessible, such as naturally occurring minerals. In this context, we propose the use of natural vermiculite clay, which we have found to be a 2D antiferromagnetic wide band gap semiconductor. Vermiculite[5,6] is a member of the layered silicate family which has already demonstrated its potential in applications[7], such as antibiotics capture[8], CO_2 absorption[9], or water purification[10]. Vermiculite is traditionally known for its fire resistance and use in insulation and construction[5], it also has more advanced applications in electronic devices as we demonstrate here[1]. Indeed, vermiculite can be combined with semiconducting materials for photocatalysis, forming vermiculite-photoactive compound heterostructures[11,12]. Vermiculite is widely available, with world-wide reserves at 600 million tons, with the main producers in South Africa, United States, Brazil, Russia, China, Australia[13–15].

[1]Department of Physics, Norwegian University of Science and Technology – NTNU, Trondheim, Norway. [2]Instute of Physics, University of Sao Paulo – USP, Sao Paulo, Brazil. [3]Swiss Norwegian Beamlines at European Synchrotron Radiation Facility, Grenoble, France. [4]Department of Inorganic Chemistry, Faculty of Science, Charles University, Prague, Czech Republic. ✉e-mail: barbara.pacakova@ntnu.no; jon.fossum@ntnu.no

Fig. 1 | Macroscopic and crystal structure of Vermiculite. a Vermiculite crystals as received displayed on the scale of mm-cm. **b** Vermiculite crystal structure, with the unit cell highlighted with black lines. Comparison with the synthetic fluorhectorite clay is shown in Supplementary Fig. 1.
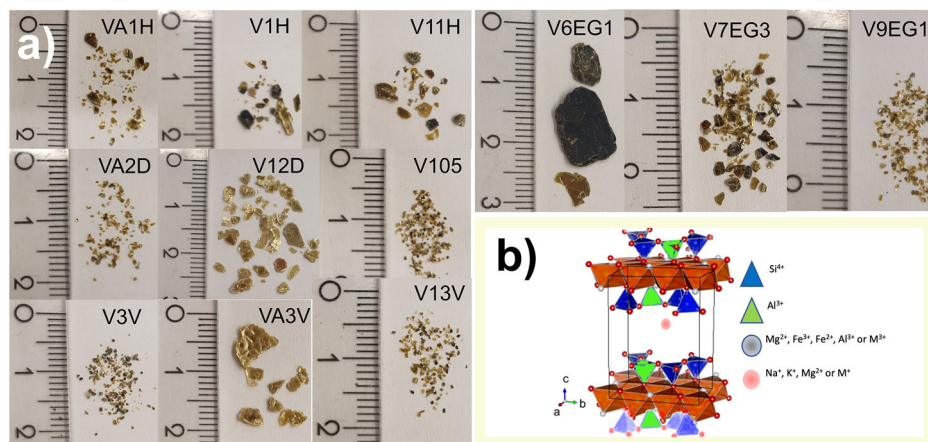
Even if 3D magnetic materials have been implemented in conventional devices, their applications in spintronics and nanoscale electronics are severely restricted due to their large dimensions.

Antiferromagnetism offers several advantages for spintronic applications, including non-responsiveness to external perturbations of magnetic field, fast spin dynamics, and spin packing density and absence of any stray field[16]. This could lead to more robust and efficient devices compared to the ones based on ferromagnetic materials. Furthermore, as the resulting zero net magnetic moment makes magnetism in antiferromagnets externally invisible, information stored in magnetic moments would also be invisible to common magnetic probes. Also, their insensitivity to disturbing magnetic fields, and the antiferromagnetic element would maintain magnetic stability among neighboring elements, regardless of how densely the elements are arranged in the device[17]. Furthermore, 2D antiferromagnetic materials[18] can also act as efficient spin filters. They provide an effective way to overcome limitations in thin films made from traditional 3D materials and offer potential for more advanced 2D devices in the nanoscale regime[16,18,19].

A natural vermiculite nanolayered particle[5,6,20] is a 2:1 phyllosilicate, consisting of 0.95 nm thin, negatively charged single nanosheets[21,22], kept together in nanolayered stacks by electrostatic interactions via charge compensating cations present in the interlayers. Each individual nanosheet is composed of sub-sheets of two types – two tetrahedral sheets sandwiching one octahedral sheet (see Fig. 1 and Supplementary Fig. 1). All tetrahedra and octahedra have metals inside: Al and Si in case of the tetrahedral sheets and Al, Mg and/or divalent or trivalent metallic M^{2+} and M^{3+} ions in the octahedral sheets. Vermiculite can be found in two different composition types, dioctahedral or trioctahedral, with effective sheet surface charges ranging from about 0.6 to 1.0 electron charges per half lateral unit cell, often denoted charge per formula unit, pfu. Interlayer cations are exchangeable[23,24] if the charge is sufficiently low and below 0.6–0.7 pfu. In nature, more complex structures can be found, with multiple metals occupying octahedral sheets, varying based on their geographic origin, with combination of Mg, Al, Fe^{3+}; Fe^{2+}, Ti and Mn; also with a combinations of divalent and single valent cations in the interlayers[20,25].

Swelling layered materials like vermiculite can exhibit three hydration states—0, 1, or 2 water layer (WL) hydrates—depending on the hydration enthalpy of the interlayer cation[24]. Swelling layered silicates can typically be delaminated into single nanosheets[24,26] and dispersion of single nanosheets in liquid (such as water or organic solvents) allows large scale self-assembly production of layered nanocomposites, heterostructures or formation of self-standing thin films. This capability is crucial for electronic devices as it facilitates the scalable manufacturing of intricate and high-performance materials, opening up for the development and integration of advanced electronic components.

However, delamination into single vermiculite nanosheets is challenging due to nonuniform and/or high charge distribution caused by structural defects and impurities. Consequently, the practical delamination of vermiculite[7,27–31] is significantly more difficult as compared to low-charge[22] clay minerals such as montmorillonite or hectorite, for which the surface charge is typically in the range of 0.2–0.5 pfu[24].

Aware of the challenges related to vermiculite exfoliation, we have used an effective approach for converting vermiculite into single nanosheets. We decided to use liquid exfoliation process, as it preserves the compactness of the nanosheets, in ideal case the size of the nanosheet is the single crystal or larger polycrystal, and it is not chopped to smaller sizes. One of the largest yields of exfoliation processes reported, which also preserves the exfoliated sheet quality is intermediate- assisted grinding exfoliation[32], but we chose liquid exfoliation, which can also provide very large yields[33], as it is simple and it can be used in any laboratory. We used the vermiculite swelling ability in hydrogen peroxide (H_2O_2), dimethyl sulfoxide (DMSO), di-methyl formamide (DMF) and N-methyl formamide (NMF), and further mechanical treatment using sonification. We demonstrate that the types of interlayer cations in 12 different vermiculite samples heavily influence their ability to delaminate into single nanosheets. In our efforts toward vermiculite-based electronics, we took the exfoliated material and measured the band gap, demonstrating that it is a large band-gap semiconductor, and we support this by simulations. Our findings thus highlight the potential of natural vermiculite for electronic and photonic applications, offering an under-explored and unexploited avenue for the efficient, scaled-up fabrication of 0.95 nm-thin semiconducting nanosheets, providing a sustainable alternative to synthetic wide band gap semiconductors.

Results

Twelve different types of vermiculite samples from different sources were investigated (see Supplementary Table 1 and Materials and methods section). We tested several organic solvents to delaminate vermiculite into nanosheets, trying to keep delamination as easy as possible, thus allowing large-scale production of delaminated vermiculite. If the interlayers of vermiculite contain hydratable cations (such as Na^+ and Mg^{2+}), its affinity to water and other organic solvents causes osmotic swelling and subsequent delamination into single nanosheets[22,24,30]. To evaluate the possibility of exfoliation into single nanosheets, information of the elemental composition of interlayer cations is needed, as there can be natural non-hydratable cations present in the structure.

Structure and elemental composition

Delamination of vermiculite into single nanosheets is typically impossible without any pre-treatment[31]. To determine cation species in the interlayers, providing suggestions which of the vermiculites are easily exfoliable, we used XPS, Mossbauer spectroscopy and synchrotron XRD (SXRD, see Supplementary Figs. 2–15 and Supplementary Tables 2–7). XPS showed all the elements present, with the spectral line attributions given in Supplementary

Figs. 6–12. All samples contained Fe^{3+} and minor amount of Fe^{2+}, as was determined by Mossbauer spectroscopy (Supplementary Fig. 16 and Supplementary Tables 6–7). The SXRD diffraction patterns combined with XPS resolved the location of iron within the vermiculite structure, distinguishing whether it is in the octahedral layers or in the interlayers. Since we observed no hydration states in the interlayers corresponding to interlayer iron, our findings indicate that all our vermiculite samples are in the trioctahedral form (Supplementary Section 3 in Supplementary).

In the first step, we cation exchanged as received vermiculites with Na^+. This step has been reported also lately[33]. To determine which ion species are left in the interlayer after Na^+ exchange, we compared SXRD patterns of the samples exposed to humid atmosphere with the corresponding dry samples (Supplementary Tables 2 and 3). Detail explanation of how to determine which ions are present in the interlayers is in the Supplementary section 3. We mainly focused on the (001) diffraction peak, which is a measure of the distance between two vermiculite nanosheets kept together by (hydratable) interlayer cations. We observed that most of the samples exhibited 1WL hydrated Na^+. However, as described in the Supplementary (Supplementary Section 3, Supplementary Tables 1, 2, Supplementary Fig. 2), we found other types of cations and species in addition to Na^+, such as K^+, Mg^{2+} and $Mg(OH)_2$. This evidenced that as expected, that not all interlayer cations in original samples were replaced. The reason why not all original ions are replaced is the inhomogeneous layer surface charge of this natural clay. We observed multiple (001) peaks in the diffraction patterns, indicating different hydration states of various cation species, as is described in Supplementary Tables 1, 2 and Supplementary Fig. 2. This suggests that the cations are not homogeneously dispersed within the individual interlayers. Instead, we have 'stacks' of nanosheets with predominantly one type of cation per stack. If multiple cations were dispersed within single interlayers, we would not observe distinct (001) peaks.

Intercalation of solvents and delamination

After hydration of the interlayer or intercalation of solvent, especially in the case of Na^+, individual nanosheets might be delaminated by osmotic swelling[22,24]. However, as the layer charge of vermiculite is up to several times higher than the surface charge of typical swelling clay minerals, delamination of single sheets is very difficult, thus requiring use of other solvents than water, for instance DMSO, DMF or NMF (for schematics of intercalation and further delamination, see Fig. 2)[31].

To scale-up delamination process, we exposed powder vermiculite samples, not the original crystals, to these organic solvents. We observed solvent intercalation for all samples in the powder form (Supplementary Table 4 and Supplementary Figs. 3–5). Among tested organic solvents, only DMSO has the advantage of being non-toxic and environmentally friendly, so we used it for the further delamination process. Swelling of the interlayers in these solvents was investigated using SXRD. We tested 12 dilutions of DMSO with water, ranging from 5 to 100% of DMSO. Examples from 2 selected samples-VA1H and V10_5 are displayed in Fig. 3. We chose these

samples for up-scaled delamination for two reasons: the V10_5 sample contains just Na^+ and $Mg(OH)_2$ and no other cations, so cation exchange with Na^+ was complete; and VA1H as it contains just wettable cations – Na^+ and Mg^{2+}, meaning it has low charge and fully swells in a DMSO/water mixture (see Fig. 3 and Supplementary Figs. 3–5). The d-spacing changes of the (001) diffraction peak is dependent on the DMSO:water ratio. Up to 72% of DMSO in water in the case of VA1H sample (Fig. 3a) and 60% for the V10_5 sample, interlayer of vermiculite is intercalated with 1 layer of DMSO. Above these concentrations up to pure DMSO, there are 2 molecules of DMSO in the interlayer. In all cases[34], DMSO/water at all concentrations intercalates into the vermiculite powder within 30 s. As DMSO does not affect the quality of the nanosheets, which is evident from preservation of in-plane SXRD diffraction peaks, DMSO proves to be an ideal substance for delamination of vermiculite into single nanosheets.

After swelling of the samples in pure DMSO for 2 days, followed by mechanical treatment using ultrasonication, we delaminated vermiculite into single nanosheets, with approximately 70% yield for both samples (see AFM images, Fig. 3 and Supplementary Fig. 17). As the powders were grained manually from the large vermiculite crystals, the yield is expected to increase by making the powders finer. The AFM measurement of individual nanosheets showed that it is 0.25 nm larger than the real thickness (1.2 nm), as a result of one water layer under the nanosheets, as is typical for all deposited 2D materials from suspension[35,36]. This value is in accordance with the AFM thickness of for instance fluorohectorite clay (Supplementary Fig. 1)[24,37]. During delamination, we did not preserve the size of the nanosheets as was their macroscopic size in grained powder– nanosheets always brake on the grain boundaries, so single nanosheets are single crystals as well. This is typically observed for synthetic fluorohectorite clay, even when we do not use any harsh treatment, just immersing and spontaneously delaminating single nanosheets in water.

Determination of band gap

To experimentally determine the band gap of our samples, we measured UV-VIS spectra of delaminated sample, measuring dependence of the absorption on the wavelength, $\alpha(\lambda)$. Data were plotted as $(\alpha^* E)^2$ vs. E – the so called Tauc plot which can be used for the determination of direct band gap in semiconductors[38,39]. The high energy part of the curves was fitted by a linear function to determine the electronic band gap value, E_g (Fig. 4). E_g of the VA1H and V10_5 samples, giving E_g values of 3.85 and 3.93 eV, respectively. The band gap values of other samples gave $E_g = 3.3$–3.9 eV (Supplementary Figs. 19 and 20). This demonstrates that vermiculite belongs to the family of wide band gap semiconductors and that value of the band gap depends on the exact elemental composition. Two previous studies are also reporting the band gap of vermiculite determined by Tauc plot[11,13] are in agreement with our results. The band gap value of vermiculite is comparable with several synthetic wide band gap semiconductors such as oxides[40,41] TiO_2, $E_g = 3.55$ eV or ZnO, $E_g = 3.2$ eV, $SrTiO_3$, $E_g = 3.4$ eV, and
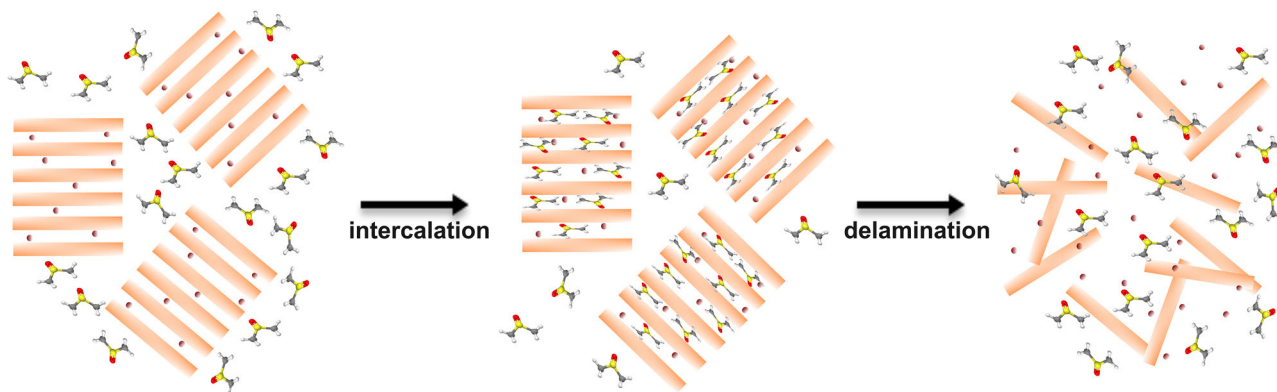

Fig. 2 | Schematics of intercalation of DMSO into stacks of vermiculite nanosheets kept together by interlayer cations and their further delamination by osmotic swelling.
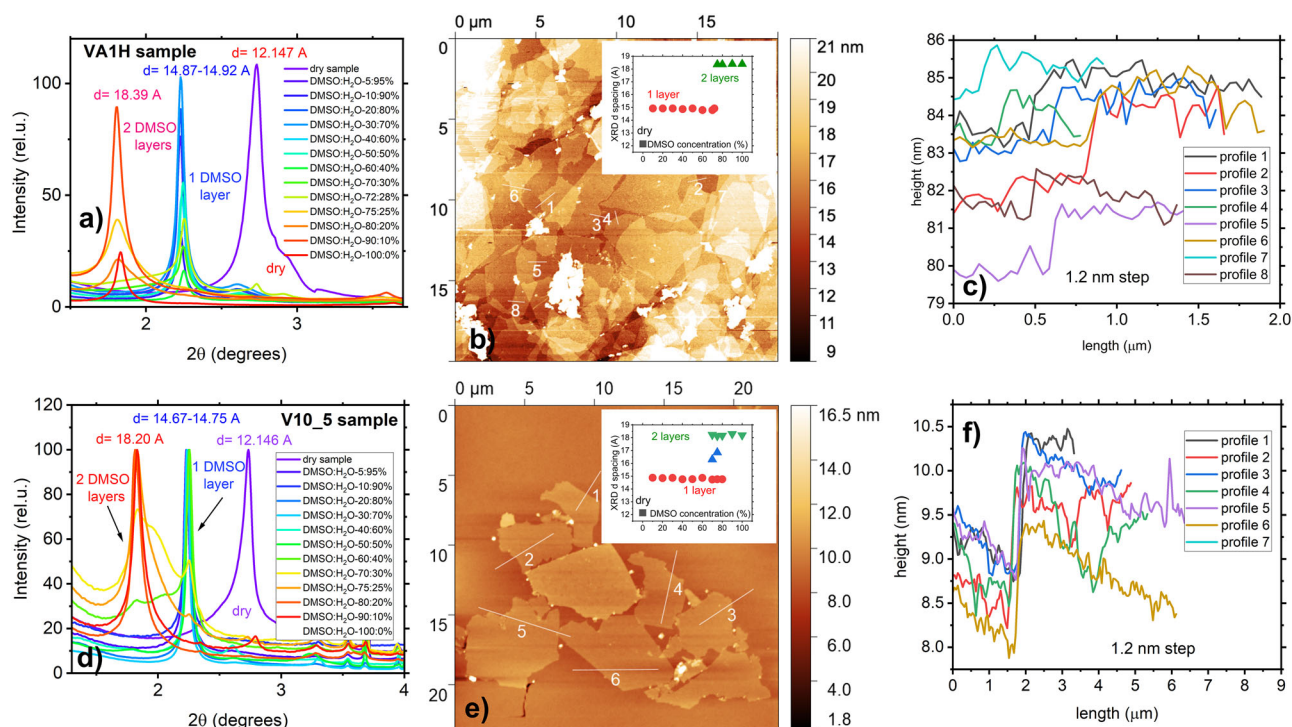
Fig. 3 | Swelling and delamination of vermiculite in DMSO. a, d The XRD pattern of intercalation of DMSO mixed with water at different ratios into the interlayer - (001) diffraction peak for dry and DMSO:H_2O exposed VA1H and V10_5 vermiculite samples, with wavelength $\lambda = 0.57986$ Å. We observe 2 distinct states for the VA1H sample (inset of **b**) – 1 layer of intercalated DMSO up to DMSO:H_2O ratio of 75:25% and 2 DMSO layers above this concentration. We also observe 2 layers of DMSO after exposure to pure solvent. In case of the V10_5 sample (inset of **e**), 1 layer of DMSO is reached up to DMSO:H_2O ratio 60:40%, and 2 intercalated layers are obtained above this concentration. We also see the intermediate state with the layer swelled in between 1-2 DMSO layers in the DMSO:H_2O concentration range 70:30–80:20%. **b, e** The AFM topography images of the VA1H and V10_5 samples showing delaminated single layers. **c, f** Cross-section images of the topography for both samples. Single layer vermiculite thickness is in both cases 1.2 nm, which corresponds to the AFM thickness of the single layer synthetic fluorohectorite clay.
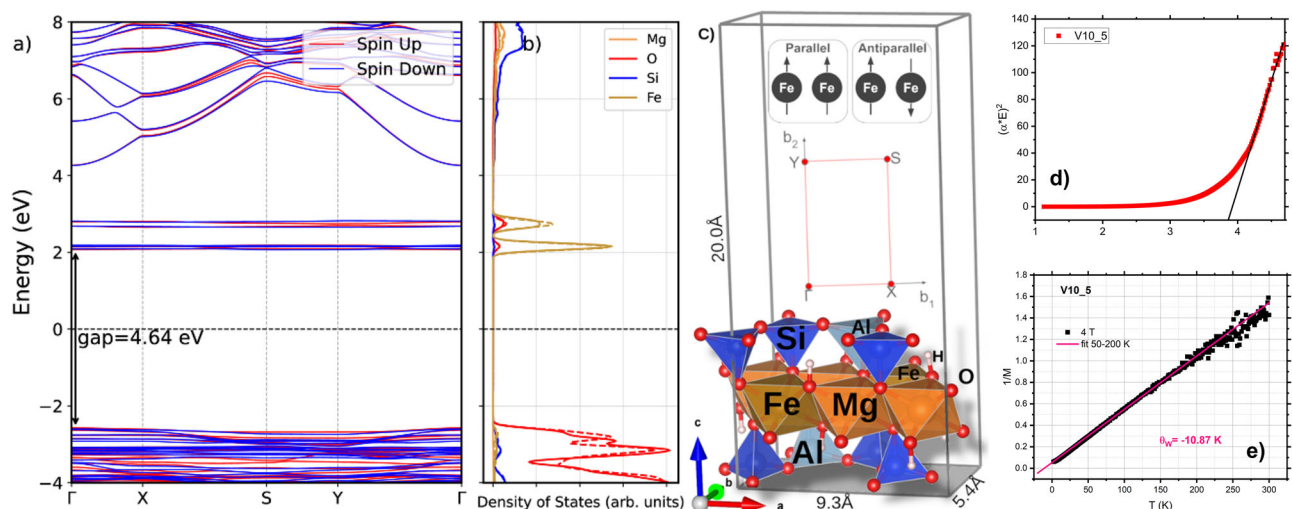

Fig. 4 | Band gap and antiferromagnetic properties of vermiculite. a Electronic band structure and **b** projected density of states results for **c** vermiculite slab simulation cell used in the DFT-HSE calculations. Figure 1c illustrates the atomic composition, positional configurations, and the simulation cell used as input for the calculations. The insets also show the high-symmetry points and lines of the first Brillouin zone used in the band structure calculations (figure center), besides schematics for the initial Fe spin orientations considered to account for ferromagnetic and antiferromagnetic ordering. **d** – Tauc plots of the V10_5 sample, **e** inverse temperature dependence of magnetization at 4T with fit by Curie-Weiss law (pink).

GaN, $E_g = 3.4$ eV[42]. An advantage of the vermiculite-based material is that it can serve as a cheap and sustainable natural alternative to these standard synthetic materials. This is particularly promising as the challenging exfoliation process for this system is mastered not only by us, but by several different approaches[30,31].

Building on experimental insights, our DFT calculations also confirm that vermiculite is a wide-band gap semiconductor. Using the HSE approach for more accurate band gap estimation, we identified a band gap of 4.6 eV (Fig. 4a) between the valence band, primarily composed of oxygen atoms, and the mid-gap states introduced by Fe atoms (Fig. 4b). In the pure

hectorite phase, where Al atoms are replaced by Si and Fe by Mg (see Fig. 4c), the band gap is estimated to be 7.2 eV. The introduction of Fe atoms results in localized mid-gap states, and we observed hybridization between Fe and neighboring oxygen atoms. This hybridization modifies the electronic structure by narrowing the band gap and altering the material's properties, potentially enhancing its suitability for electronic and spintronic applications.

Magnetic ordering

Regarding the magnetic ordering, we investigated ferro and anti-ferromagnetic configurations by imposing initial magnetic orientations to the Fe^{3+} atoms in DFT calculations. Both configurations showed a small energy difference in the order of 2 meV per formula unit (pfu), suggesting that vermiculite with structure that was used for our simulation scan exhibit either ferromagnetic (converged total 8.6 Bohr mag/cell) or anti-ferromagnetic (0 Bohr mag/cell) local ordering. In the literature, Ballet and Coey's[43] experimental study further supports this, showing that vermiculite can be both in ferromagnetic and antiferromagnetic ground state. At room temperature, both forms are in the paramagnetic state.

However, antiferromagnetic ground state of real selected samples, containing Fe^{3+} with little presence of Fe^{2+} (Supplementary Fig. 16 and Supplementary Tables 6, 7), is experimentally found from fitting the temperature dependence of inverse magnetization at 4 T by Curie-Weiss law. Example is in Fig. 4d, with fitted Curie-Weiss constant $\theta_w = -10.87$ K for the V10_5 sample, as an imprint of antiferromagnetic ordering (Fig. 4 and Supplementary Fig. 18).

Discussion

Addressing the challenges of vermiculite exfoliation, we have adapted and used an efficient method for producing single nanosheets from vermiculite. Our approach utilizes the cation exchange and swelling properties of vermiculite in organic solvents, in combination with ultrasonication mechanical treatment, to achieve effective delamination. This method significantly improves the feasibility and efficiency of exfoliating vermiculite, opening new possibilities for its use in advanced material synthesis and electronic applications.

In our pursuit of vermiculite-based electronics, we also measured the band gap of the exfoliated material, confirming that it can function as a wide band-gap semiconductor with antiferromagnetic ground state. This finding, supported by both experimental data and simulations, is crucial for the development of future technologies that require wide band gap semiconductors for electronic nanodevices operating at high frequencies or voltages. However, our DFT simulations show that band structure of vermiculite is flat. Flat bands play an important role in physics of topological electrons. From the point of applications in electronics, it in principle hinders transport due to the zero-group velocity, even for the semiconductor. In contrary, they are very important in correlated quantum matter and photonic latices[44]. Flat-band have promising applications in photonic systems[45–48]. The zero-group velocity in flat bands can be used to achieve slow light[49,50], and enhanced light-matter interaction[48]. However, our simulations are not done for the real structure of vermiculite as we determined from our experiments, but idealized structure of vermiculite containing just Fe^{3+}. As we know there is also Fe^{2+} present in the structure, this will lead to narrowing of the band gap simultaneously with changing of the band structure, so theoretical values will get closer to those we observed for different vermiculite samples (Supplementary).

Our study not only enhances the understanding of vermiculite exfoliation but also highlights the potential of natural vermiculite in creating sustainable and high-performance nanoelectronics/photonics and importance in correlated quantum matter. With its natural abundance, affordability, non-toxicity, and the ability to be exfoliated into high-quality nanosheets, vermiculite emerges as a promising candidate for future electronic and spintronic devices.

Methods

Vermiculite samples - origin and cation exchange with Na

We acquired 12 different vermiculite samples, with origin in Denmark, USA and Canada, with particle sizes in the range of 1–>30 mm (see Fig. 1). We investigated three batches of samples: 'Virginia' from Virginia Vermiculite Ltd. 'Elk Gulch' from Elk Gulch valley in Montana, USA, 'Denmark' series from sites in Denmark and 'Hindman' series from various locations in USA and Canada. For details see the Supplementary Table 1.

All vermiculite samples were cation exchanged using NaCl, thus partly replacing interlayer cations with Na+. The protocol used was as follows: first, powder samples were rinsed with deionized water, and then cation exchanged using a saturated NaCl solution, heating the samples at 70–120 °C for 1, 9.5 and 12 h, depending on the type of sample type (see Supplementary Table 1). To remove remaining excess cations from the solution after cation exchange, the powder samples were dialyzed. For schematics of synthesis, see Fig. 2.

Synchrotron X-ray diffraction (SXRD)

SXRD experiments were done at the Swiss-Norwegian beamline BM01 at ESRF, Grenoble, France, in transmission mode using PILATUS3 X_2M detector, wavelength of X-ray beam was 0.57986 Å.

To determine the type of the vermiculite (dioctahedral or trioctahedral), and type of interlayer cation (K^+, Na^+, Mg^{2+}), two kinds of sample preparations were employed - samples containing 1 WL in the interlayers and samples exposed to in-situ drying to remove any water absorbed. Vermiculite crystals were first crushed to a fine powder and loaded into glass capillaries (diameter 1 mm). Capillary were sealed with glue for the 1WL layer hydrated samples, and with glass wool for the samples prepared for in-situ drying. During the in-situ drying, samples were heated upon constant vacuum pumping using cryo-stream blower, from 50 to 120 °C with a rate 60 K/hour and kept at 120 degrees for a time which was necessary for complete drying of the interlayer. Complete drying was identified as the state when diffraction pattern (position of (001) peak) was not changing within time span of 10 min.

Dry samples were subsequently exposed to either liquid DMF, NMF, DMSO, or a DMSO/water solution to study their in-situ swelling capabilities in these solvents.

Data were processed and analyzed using Bubble[51], MEDVED[52] and Fullprof[53] software.

Exfoliation of powder vermiculite into single nanosheets assisted by DMSO, DMF and NMF

Vermiculite crystals were ground in a mortar to a very find powder. Then, we isolated 150 mg of powder which was immersed in 5 ml of DMSO and magnetically stirred at 450 rpm for 2 days. 5 ml of water was added after 2 days, and the sample was ultrasonicated for 30 min to induce mechanical delamination of sheets. Samples in the water-DMSO solutions were subsequently diluted 1:1000 and deposited on plasma treated SiO_2(100 nm)@Si substrates to verify exfoliation into single sheets by AFM.

Atomic force microscopy

Atomic force microscopy (AFM) of single layer (SL) vermiculite nanosheets deposited on plasma treated SiO_2(100 nm)@Si substrates were done with a Multimode III (Veeco – Bruker) SPM with Nanoscope IV controller in tapping mode. TAP 150-G cantilevers (BudgetSensors) with resonant frequency $f_0 = 150$ kHz, tip radius <10 nm and RTESP-150 probes with $f_0 = 150$ kHz (Bruker probes) were used, keeping comparable wear of the tips. Optical images of single layers were captured with a Nikon microscope mounted as a standard visualization tool in the Multimode III SPM. AFM images were processed in Gwyddion software[54], processing the image by 1st order flattening and scars removal. From the cross-sections of layers on substrate, we determined thickness of the nanosheets.

Article

XPS measurements

XPS spectra were recorded for samples under vacuum at room temperature in vacuum chamber using a SES2002 spectrometer (Scienta) in conjunction with a monochromatized Al Kα X-ray source (Scienta). An energy resolution of about 0.4 eV was obtained at 200 eV pass energy. Powders made from all samples were deposited on the carbon double-side tape. Captured spectra were processed using Matlab, using the Shirley baseline correction and refinement of peaks attributed to C1s and N1s, respectively.

Mossbauer spectroscopy

^{57}Fe Mössbauer spectroscopy was carried out on a Wissel spectrometer using transmission geometry and a proportional detector at ambient temperature without an applied magnetic field. The velocity calibration of the Wissel spectrometer was performed using a standard alpha–Fe foil. Mössbauer spectra were fit using the Wissel NORMOS routine.

UV-VIS spectroscopy

UV-VIS spectra were measured with the Agilent 8453 spectrometer in the range 190–1100 nm. Vermiculite nanosheets in DMSO:H_2O solution with concentration 1:1 were examined. As a blank sample, we used DMSO:H_2O mixture with 1:1 ratio. Original absorption-wavelength $a(l)$ dependence was re-plotted as $(a*E)^2$ vs. E, the so-called Tauc plot used for determination of the direct band gap in semiconductors[38,39]. High energy part of curves was fitted by linear dependence to determine electronic band gap value, E_g.

Magnetic properties measurements

Magnetic properties of samples were measured using MPMS7 device from Quantum Design in High magnetic field laboratory (MGML), Charles university in Prague, Czech Republic.

Temperature dependence of magnetization was measured at 4T. Recalculated temperature dependence of inverse susceptibility was fitted by the Curie-Weiss law that provided value of the Curie constant.

DFT simulations

To support the experimental findings of band gap width, we perform first-principles calculations based on the Density Functional Theory (DFT)[55,56] to investigate the electronic structure and properties of the vermiculite system.

The Quantum ESPRESSO[57] package was our primary computational tool. We leverage the hybrid Heyd-Scuseria-Ernzerhof (HSE)[58,59] exchange-correlation functional, which is known for its enhanced accuracy in predicting the electronic properties of semiconductors and insulators compared to standard DFT methods. This choice is motivated by the need for a more precise description of the exchange and correlation effects, which are crucial for the systems and properties under study. HSE is known for its enhanced accuracy in predicting the energy gap of semiconductors and insulators compared to standard DFT methods. This functional was selected to provide a more precise description of the exchange and correlation effects, which are critical for accurately modeling the systems and properties under study. To model the electron-ion interactions accurately, we used norm-conserving standard Siesta pseudopotentials, which efficiently handle the core electrons while explicitly treating the valence electrons. The calculations were performed using a double-zeta polarized (DZP) basis set, with a mesh cut-off of 300 Ry to ensure adequate representation and convergence of the kinetic energy of the electrons in our simulations.

The calculations were performed with fully relaxed atomic positions and cell dimensions to ensure the system reached its ground state. The relaxed orthorhombic crystal dimensions were 9.3 Å × 5.4 Å × 20.0 Å. In the reciprocal space, we used a Monkhorst-Pack k-point grid of 4 × 8 × 1 to accurately sample the Brillouin zone. We investigated both ferromagnetic and antiferromagnetic electronic configurations by assigning different initial magnetic moments (parallel and antiparallel) to the two Fe neutral atoms in the unit cell, then allowing the system to converge to its energetically preferred magnetic moment.

References

1. Barcelos, I. D. et al. Phyllosilicates as earth-abundant layered materials for electronics and optoelectronics: Prospects and challenges in their ultrathin limit. *J. Appl. Phys.* **134**, 090902 (2023).
2. Pearton, S. J. et al. Wide band gap ferromagnetic semiconductors and oxides. *J. Appl Phys.* **93**, 1–13 (2003).
3. Tsao, J. Y. et al. Ultrawide-Bandgap Semiconductors: Research Opportunities and Challenges. *Adv. Electron Mater.* **4**, 1600501 (2018).
4. Wei, X. P. et al. Electronic, magnetic and transport properties of antiferromagnetic semiconductor BaGd2X4(X[dbnd]S, Se). *Mater. Sci. Semicond. Process* **169**, 107856 (2024).
5. Martynková, G. S. & Valášková, M. Vermiculite in Nanocomposites. In: *Encyclopedia of Nanoscience and Nanotechnology*. (American scientific publishers, 2009).
6. Bergaya, F., Lagaly, G. & Brigatti, M. F. *Handbook of Clay Science* (Elsevier, 2006).
7. Nicolosi, V., Chhowalla, M., Kanatzidis, M. G., Strano, M. S. & Coleman, J. N. Liquid Exfoliation of Layered Materials. *Science (1979)* **340**, 1226419 (2013).
8. Valdés, L. et al. A simple way for targeted delivery of an antibiotic: In vitro evaluation of a nanoclay-based composite. *PLoS One* **12**, e0187879 (2017).
9. Cavalcanti, L. P., Kalantzopoulos, G. N., Eckert, J., Knudsen, K. D. & Fossum, J. O. A nano-silicate material with exceptional capacity for CO2 capture and storage at room temperature. *Sci. Rep.* **8**, 11827 (2018).
10. Mahapatra, P. L. et al. A comprehensive review of atomically thin silicates and their applications. *2D Materials* **11**, 032003 (2024).
11. Zhang, J., Liu, T., Chen, R. & Liu, X. Vermiculite as a natural silicate crystal for hydrogen generation from photocatalytic splitting of water under visible light. *RSC Adv.* **4**, 406–408 (2014).
12. Wan, Y. et al. A review of recent advances in two-dimensional natural clay vermiculite-based nanomaterials. *Mater. Res. Express* **6**, 102002 (2019).
13. Huang, Z. et al. 2D Functional Minerals as Sustainable Materials for Magneto-Optics. *Adv. Mater.* **34**, 1–8 (2022).
14. Map of world vermiculite production. https://www.mapsofworld.com/minerals/world-vermiculite-producers.html (2022).
15. United States Geological Survey (USGS) Minerals Resources Program. Vermiculite production by countries. https://www.indexmundi.com/minerals/?product=vermiculite&graph=production (2013).
16. Rahman, S., Torres, J. F., Khan, A. R. & Lu, Y. Recent Developments in van der Waals Antiferromagnetic 2D Materials: Synthesis, Characterization, and Device Implementation. *ACS Nano* **15**, 17175–17213 (2021).
17. Hu, G. & Xiang, B. Recent Advances in Two-Dimensional Spintronics. *Nanoscale Res Lett* **15**, 226 (2020).
18. Jungwirth, T., Marti, X., Wadley, P. & Wunderlich, J. Antiferromagnetic spintronics. *Nat. Nanotechnol.* **11**, 231–241 (2016).
19. Elahi, E. et al. A review on two-dimensional (2D) magnetic materials and their potential applications in spintronics and spin-caloritronic. *Comput. Mater. Sci.* **213**, 111670 (2022).
20. McL. Mathieson, A. & Walker, F. G. Crystal Structure of Magnesium-Vermiculite. *Am. Mineralogist J. Mineralogical Soc. Am.* **39**, 231–255 (1954).
21. Stoter, M. et al. Controlled Exfoliation of Layered Silicate Heterostructures into Bilayers and Their Conversion into Giant Janus Platelets. *Angew. Chem. Int. Ed.* **55**, 7398–7402 (2016).

22. Rosenfeldt, S. et al. In-Depth Insights into the Key Steps of Delamination of Charged 2D Nanomaterials. *Langmuir* **32**, 10582–10588 (2016).

23. Suzuki, M., Wada, N., Hines, D. R. & Whittingham, M. S. Hydration states and phase transitions in vermiculite intercalation compounds. *Phys. Rev. B* **36**, 2844–2851 (1987).

24. Stöter, M., Rosenfeldt, S. & Breu, J. Tunable Exfoliation of Synthetic Clays. *Annu. Rev. Mater. Res* **45**, 129–151 (2015).

25. Valkov, M. & Simha, G. Vermiculite: Structural Properties and Examples of the Use. *Clay Minerals in Nature - Their Characterization, Modification and Application*, https://doi.org/10.5772/51237 (2012).

26. Fossum, J. O. Clay nanolayer encapsulation, evolving from origins of life to future technologies. *Eur. Phys. J. Spec. Top.* **229**, 2863–2879 (2020).

27. Nicolosi, V., Chhowalla, M., Kanatzidis, M. G., Strano, M. S. & Coleman, J. N. Liquid exfoliation of layered materials. *Science* **340**, 72–75 (2013).

28. Shao, J.-J., Raidongia, K., Koltonow, A. R. & Huang, J. Self-assembled two-dimensional nanofluidic proton channels with high thermal stability. *Nat. Commun.* **6**, 7602 (2015).

29. Udoudo, O., Folorunso, O., Dodds, C., Kingman, S. & Ure, A. Understanding the performance of a pilot vermiculite exfoliation system through process mineralogy. *Min. Eng.* **82**, 84–91 (2015).

30. Dudko, V. et al. Delamination by Repulsive Osmotic Swelling of Synthetic Na-Hectorite with Variable Charge in Binary Dimethyl Sulfoxide-Water Mixtures. *Langmuir* **38**, 10781–10790 (2022).

31. Dudko, V. et al. Spontaneous delamination of affordable natural vermiculite as a high barrier filler for biodegradable food packaging. *Mater. Adv.* **3**, 9052–9062 (2022).

32. Zhang, C. et al. Mass production of 2D materials by intermediate-assisted grinding exfoliation. *Natl Sci. Rev.* **7**, 324–332 (2020).

33. Huang, Z. et al. An inorganic liquid crystalline dispersion with 2D ferroelectric moieties. *Natl Sci. Rev.* **11**, nwae108 (2024).

34. Pacak, P. Polarizability and molecular radius of dimethyl-sulfoxide and dimethylformamide from refractive index data. *J. Solut. Chem.* **16**, 71–77 (1987).

35. Verhagen, T., Klimes, J., Pacakova, B., Kalbac, M. & Vejpravova, J. Anomalous freezing of low-dimensional water confined in graphene nanowrinkles. *ACS Nano* **14**, 15587–15594 (2020).

36. Li, Q., Song, J., Besenbacher, F. & Dong, M. Two-dimensional material confined water published as part of the accounts of chemical research special issue '2d nanomaterials beyond Graphene'. *Acc. Chem. Res.* **48**, 119–127 (2015).

37. Stoter, M. et al. Nanoplatelets of Sodium Hectorite Showing Aspect Ratios of ≈20 000 and Superior Purity. *Langmuir* **29**, 1280–1285 (2013).

38. Klein, J. et al. Limitations of the Tauc Plot Method. *Adv. Funct. Mater.* **33**, 1–19 (2023).

39. Tauc, J. Optical Properties of Amorphous Semiconductors. In *Amorphous and Liquid Semiconductors* (ed. Tauc, J.) 159–220. https://doi.org/10.1007/978-1-4615-8705-7_4 (Springer US, Boston, MA, 1974).

40. Jian, J. & Sun, J. A Review of Recent Progress on Silicon Carbide for Photoelectrochemical Water Splitting. *Solar RRL* **4**, 2000111 (2020).

41. Xie, S., Zhang, Q., Liu, G. & Wang, Y. Photocatalytic and photoelectrocatalytic reduction of CO2 using heterogeneous catalysts with controlled nanostructures. *Chem. Commun.* **52**, 35–59 (2016).

42. Roccaforte, F. et al. Emerging trends in wide band gap semiconductors (SiC and GaN) technology for power devices. *Microelectron. Eng.* **187–188**, 66–77 (2018).

43. Ballet, O. & Coey, J. M. D. Magnetic properties of sheet silicates; 2:1 layer minerals. *Phys. Chem. Min.* **8**, 218–229 (1982).

44. Yang, J. et al. Realization of all-band-flat photonic lattices. *Nat. Commun.* **15**, 1–7 (2024).

45. Leykam, D., Andreanov, A. & Flach, S. Artificial flat band systems: From lattice models to experiments. *Adv. Phys. X* **3**, 677–701 (2018).

46. Vicencio Poblete, R. A. Photonic flat band dynamics. *Adv Phys X* **6**, 1878057 (2021).

47. Leykam, D. & Flach, S. Perspective: Photonic flatbands. *APL Photonics* **3**, 070901 (2018).

48. Yang, Y. et al. Photonic flatband resonances for free-electron radiation. *Nature* **613**, 42–47 (2023).

49. Noda, S., Yokoyama, M., Imada, M., Chutinan, A. & Mochizuki, M. Polarization mode control of two-dimensional photonic crystal laser by unit cell structure design. *Science* **293**, 1123–1125 (2001).

50. Li, J., White, T. P., O'Faolain, L., Gomez-Iglesias, A. & Krauss, T. F. Systematic design of flat band slow light in photonic crystal waveguides. *Opt. Express* **16**, 6227 (2008).

51. Dyadkin, V., Pattison, P., Dmitriev, V. & Chernyshov, D. A new multipurpose diffractometer PILATUS@SNBL. *J. Synchrotron Radiat.* **23**, 825–829 (2016).

52. Chernyshov, D., Dyadkin, V., Van Beek, W. & Urakawa, A. Frequency analysis for modulation-enhanced powder diffraction. *Acta Crystallogr. A Found. Adv.* **72**, 500–506 (2016).

53. Rodríguez-Carvajal, J. Recent advances in magnetic structure determination by neutron powder diffraction. *Phys. B Condens. Matter.* **192**, 55–69 (1993).

54. Nečas, D. & Klapetek, P. Gwyddion: an open-source software for SPM data analysis. *Cent. Eur. J. Phys.* **10**, 181–188 (2012).

55. Hohenberg, P. & Kohn, W. Inhomogeneous Electron Gas. *Phys. Rev.* **136**, B 846–B 871 (1964).

56. Kohn, W. & Sham, L. J. Self-Consistent Equations Including Exchange and Correlation Effects. *Phys. Rev.* **140**, A 1133–A 1138 (1965).

57. Giannozzi, P. et al. QUANTUM ESPRESSO: A modular and open-source software project for quantum simulations of materials. *J. Phys. Condensed Matter* **21**, 395502 (2009).

58. Heyd, J., Scuseria, G. E. & Ernzerhof, M. Hybrid functionals based on a screened Coulomb potential. *J. Chem. Phys.* **118**, 8207–8215 (2003).

59. Heyd, J., Scuseria, G. E. & Ernzerhof, M. Erratum: Hybrid functionals based on a screened Coulomb potential (Journal of Chemical Physics (2003) 118 (8207)). *J. Chem. Phys.* **124**, 219906 (2006).

Acknowledgements

Author contributions

B.P. prepared samples, performed delamination, XPS, SXRD, AFM measurements, magnetic properties measurements, processed data, prepared selected figures and wrote manuscript. B.L.D. and V.O. participated at delamination of the samples and laboratory X-ray diffraction. A.K. performed DFT simulations, co-wrote the manuscript and prepared selected figures. H.D. contributed to SXRD experiments. Ch.F. and D.C. contributed to and supervised SXRD experiments. D.Z. did Mossbauer spectroscopy measurements and analysis of Mossbauer data. C.R.M., S.R. and J.O.F. supervised research. All authors commented to and approved the final version of manuscript.

Funding

Competing interests

The authors declare no competing interests.

Additional information

Supplementary information The online version contains supplementary material available at
https://doi.org/10.1038/s41699-025-00561-5.

Correspondence and requests for materials should be addressed to Barbara Pacakova or Jon Otto Fossum.

Reprints and permissions information is available at http://www.nature.com/reprints

Publisher's note Springer Nature remains neutral with regard to jurisdictional claims in published maps and institutional affiliations.